Effect of chemical substitution on the skyrmion phase in Cu_2OSeO_3

Paul M. Neves,[1,2] Dustin A. Gilbert,[1,3] Sheng Ran,[1,2] I-Lin Liu,[1,2] Shanta Saha,[2] John Collini,[1,2] Markus Bleuel,[1] Johnpierre Paglione,[2] Julie A. Borchers,[1] and Nicholas P. Butch[1,2,*]

[1]*National Institute of Standards and Technology Center for Neutron Research, Gaithersburg, Maryland 20878, USA*
[2]*University of Maryland, College Park, College Park, Maryland 20742, USA*
[3]*Department of Materials Science and Engineering, University of Tennessee, Knoxville, Tennessee 37996, USA*

(Received 10 September 2019; revised 20 August 2020; accepted 22 September 2020; published 9 October 2020)

Magnetic skyrmions have been the focus of intense research due to their unique qualities which result from their topological protections. Previous work on Cu_2OSeO_3, the only known insulating multiferroic skyrmion material, has shown that chemical substitution alters the skyrmion phase. We chemically substitute Zn, Ag, and S into powdered Cu_2OSeO_3 to study the effect on the magnetic phase diagram. In both the Ag and the S substitutions, we find that the skyrmion phase is stabilized over a larger temperature range, as determined via magnetometry and small-angle neutron scattering (SANS). Meanwhile, while previous magnetometry characterization suggests two high temperature skyrmion phases in the Zn-substituted sample, SANS reveals the high temperature phase to be skyrmionic while we are unable to distinguish the other from helical order. Overall, chemical substitution weakens helical and skyrmion order as inferred from neutron scattering of the $|q| \approx 0.01$ Å^{-1} magnetic peak.

DOI: 10.1103/PhysRevB.102.134410

I. INTRODUCTION

The study of quantum materials focuses on understanding the emergent properties of interacting electronic systems, including effects such as topology, and leveraging those properties to develop new technologies. Magnetic skyrmions are one such topologically protected spin arrangement [1–3]; the topological nature of skyrmions makes it extremely challenging to change the configuration, and thus makes them promising for data storage technologies [4] with a high resistance to data corruption. Additionally, the relatively strong Dzyaloshinskii-Moriya interactions and direct spin interactions make these materials interesting from a fundamental condensed matter magnetism perspective [3].

One especially interesting skyrmion material is Cu_2OSeO_3 [5–7]. Being the only known insulating, skyrmion material makes it particularly attractive for low energy and high frequency spintronic devices [8,9], but the temperature and field range of the high temperature skyrmion phase is small, occurring at $T \approx 57 \pm 1$ K, and $H \approx 18 \pm 6$ mT. However, a low temperature skyrmion phase and a tilted conical phase have recently been identified in this system, whose temperature and field stability is much greater than the high temperature skyrmion phase, but also more sensitive to field and temperature hysteresis [10–13]. These helical reorientations have also been seen in MnSi [14]. This rich and complex magnetic phase diagram highlights the need for further understanding of the skyrmion stability envelope in this system.

Chemical substitution is known to be a powerful approach to tuning the skyrmion phase stability. Ni substitution on the Cu site shows an enhanced skyrmion temperature range [15] while Te substitution of Se shows a reduction in the skyrmion temperature stability in bulk samples [16], and enhanced field stability and greater thickness dependence in thin films [17]. Distinct from other substitutions, Zn substitution on the Cu site reportedly splits the skyrmion phase into two discontinuous temperature ranges [18]. However, in contrast to the low temperature skyrmion phase in the parent compound [10–13], later results demonstrated that the signature of a second skyrmion phase in Zn substitutions is caused by a coexistence of two distinct stoichiometric levels of Zn, where the nominally higher Zn concentration regions of the powder sample have a lower magnetic transition temperature, and thus a lower temperature candidate skyrmion region [19]. Further work has explored the formation energy [20], pinning effects [21,22], and expanded stability of skyrmions in Zn substitutions [23].

Here we present our study of new powdered substitutions of Ag and S, and previously studied powdered Zn substitutions using magnetization and SANS. From magnetization, Zn, Ag, and S chemical substitutions all show enhanced skyrmion temperature stability with increased substitution. We compare the effects of chemical disorder in all three cases using a SANS rotation technique that can precipitate ordered skyrmion lattices in powders [24]. These results are consistent with the magnetic phase diagram indicated by magnetization measurements, except this SANS technique is unable to distinguish the lower temperature skyrmion phase in Zn substitutions from helical order. These SANS measurements also indicate that as the skyrmion temperature stability is enhanced with substitution, the skyrmion lattice simultaneously becomes increasingly disordered.

II. EXPERIMENTAL METHODS

Powdered samples of chemically substituted Cu_2OSeO_3 were prepared following previously published techniques

*nbutch@umd.edu

[25]. The constituent powders [Alfa Aesar CuO, Puratronic, 99.995% (metals basis) powder; Alfa Aesar SeO_2, Puratronic, 99.999% (metals basis) Powder/Lump; Alfa Aesar AgO, 99.9% (metals basis); Alfa Aesar CuS, 99.8% (metals basis) −200 Mesh Powder; and ESPI Metals ZnO 99.999% −200 Mesh Powder] were ground and mixed in the correct stoichiometric ratios before being sealed in evacuated quartz ampoules. The samples were then sintered at 600 °C for several days in a box furnace. Each sample was then crushed using a mortar and pestle, pressed into a pellet, and sintered two more times. Phase purity was analyzed in each sample with x-ray powder diffraction (x-ray data shown in Appendix D). Some impurities were detected in the higher substitution level samples, and especially in the sulfur samples. The 5% S and 10% Ag samples contain approximately 15% impurities, the 10% S contains $> 15\%$ impurities, all other substituted samples show $< 5\%$ impurities, and the parent sample shows approximately 1% impurities (see Appendix D). As such, labels such as "5%" and "10%" for our substituted samples throughout the text must be understood to be only nominal concentrations. However, we emphasize that the target phase likely contributes the only significant magnetic response in our measurements.

Magnetization measurements were conducted with a superconducting quantum interference device (SQUID) magnetometer at fixed temperatures in 1 K increments while stepping the field from −4 to 120 mT. All magnetization measurements were made with increasing field, and temperature changes were always performed with a field strength of less than 5 mT. The skyrmion phase can be identified by a double inflection in the DC susceptibility data [5–7,18], and measuring both temperature and field steps allows 2D contour mapping of the phase diagram.

Neutron scattering measurements were performed at the NIST Center for Neutron Research on the NG-7 30 m SANS instrument. Approximately 50 mg of powdered sample was sealed in an aluminum foil packet and then placed in the beam. Absolute scattering intensity was calculated from empty beam flux. Temperatures were controlled with a closed cycle refrigerator (CCR), and magnetic fields were applied along the neutron flight path with an open bore resistive magnet. Scattering measurements were always performed while decreasing the field from a saturation field of approximately 0.3 T. To resolve the skyrmion phase at selective fields and temperatures, the sample was rotated about the vertical axis from 0 to +90 to −90 to 0 deg approximately five times in the static magnetic field by manually turning the CCR in the magnet, and then measuring the SANS pattern.

All measurement uncertainties, unless otherwise stated, reflect a standard uncertainty of one standard deviation.

III. RESULTS AND DISCUSSION

A. Magnetization and SANS

The magnetization of Cu_2OSeO_3 upon increasing field at 57 K is shown in Fig. 1(a), and the derivative (dM/dH, where M is the magnetization and H is the applied field) in Fig. 1(b); the skyrmion phase is readily identifiable in the derivative [5–7,18]. Starting from $H = 0$, the magnetization steadily increases as the "multi-q" helical state, labeled I in the derivative

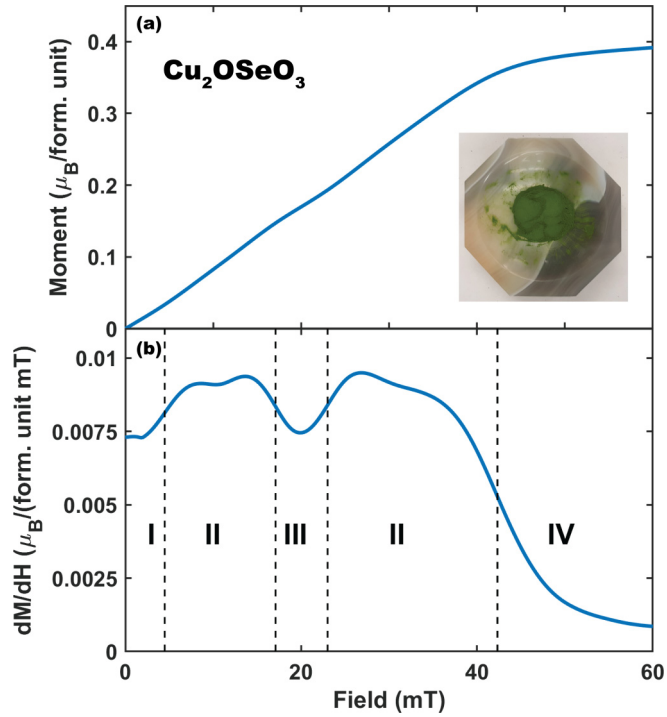

FIG. 1. Characteristic bulk magnetization for Cu_2OSeO_3 in the skyrmion phase. (a) Magnetization as a function of field for polycrystalline parent Cu_2OSeO_3 at 57 K. A photograph of the sample is included (inset). (b) The derivative dM/dH. Dashed lines mark approximate phase boundaries as determined by inflection points in dM/dH. Phase I corresponds to a multi-q helical structure, phase II represents a single-q helical structure, phase III is a Bloch-type skyrmion structure, and phase IV is a field-polarized state.

plot Fig. 1(b), deforms in response to the applied field. In this phase, helical propagation vectors are determined predominantly by magnetocrystalline anisotropy and shape anisotropy, generally preferring the {100} axes [6,26]. However, at small fields, there is a transition from a multi-q helical phase to a "single-q" helical phase (labeled II), which is marked by a sharp increase in dM/dH as the helices polarize along the field direction. The derivative then decreases again as the system enters the skyrmion phase (labeled III) as skyrmions form in the plane perpendicular to the applied field. The system then re-emerges from the skyrmion phase into the single-q helical phase with an increase in dM/dH. Finally, at high fields, the spins become field polarized (labeled IV), and dM/dH drops to near zero. These features allow rapid, rough identification of the magnetic phase boundaries. Indeed, plotting dM/dH for all of the temperatures and fields in a contour plot, Fig. 2(a), clearly emphasizes each distinct phase.

Spatially resolved techniques are required to truly characterize the nature of the magnetic order in these compounds. Standard techniques are SANS [1,8,27,28], LTEM [2,5], and x-ray microscopy and scattering [29–32]. However, these techniques traditionally require either large, high quality single crystals as in SANS, or thin films or flakes as in LTEM. Realizing samples with controlled chemical substitution is challenging in single crystals [19], but can be more easily achieved in polycrystalline samples [15,16,18,19].

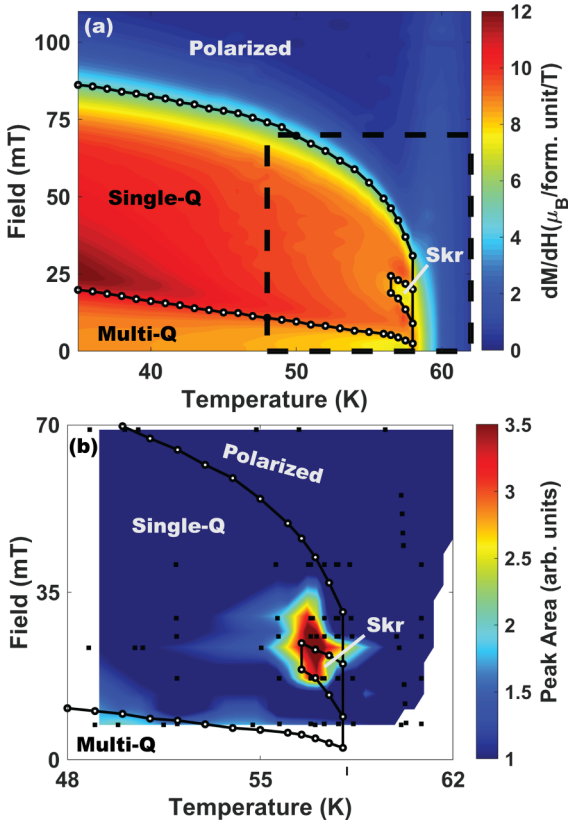

FIG. 2. Map of magnetic phase diagram from bulk magnetization and SANS. (a) dM/dH [see, for example, Fig. 1(b)] for polycrystalline parent Cu_2OSeO_3 as a function of temperature and magnetic field. Phase boundaries are indicated with black lines [determined as shown in Fig. 1(b)]. (b) The integrated intensity of magnetic SANS scattering at the $|q| \approx 0.01$ Å^{-1} peak associated with helimagnetic order. As the applied field lies parallel to the neutron beam, this map measures the helimagnetic order of the sample in the plane perpendicular to the applied field. The intense low-field and mid-field regions correspond to the multi-q helical and skyrmion phases, respectively, and agree with the phase boundaries established by the magnetization measurements from (a) (shown with black outlines). The locations of the SANS measurement points are indicated with black squares.

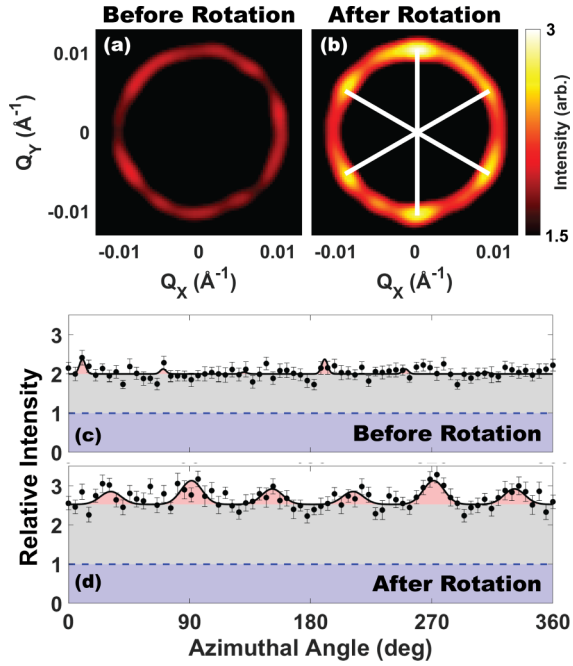

FIG. 3. Effect of rotation of skyrmions in a magnetic field on SANS pattern as reported in [24]. (a) SANS pattern of polycrystalline parent Cu_2OSeO_3 at approximately 57 K and 20 mT in the skyrmion phase (nonmagnetic structural scattering has been subtracted). No hexagonal symmetry is evident, as is shown in the corresponding annular plot averaging over $q = 0.0108 \pm 0.0024$ Å^{-1} in (c). (b) SANS signal after sample rotation (described in the text) in the 20 mT field. Hexagonal symmetry is clearly apparent (emphasized with white lines), and is further shown in the corresponding annular cut averaging over $q = 0.0108 \pm 0.0024$ Å^{-1} in (d). Both (c) and (d) show the data (black points) and fits (black lines) to Eq. (1), emphasizing how rotation enhances sixfold symmetric skyrmion lattice SANS scattering (red) on top of azimuthally uniform helimagnetic scattering (gray). The intensity in (c) and (d) is normalized to the nuclear scattering (blue). Details on the determination of each contribution to scattering are given in Appendix B. Both scattering patterns were integrated for 300 s immediately after rotation.

In powders, each grain possesses its own skyrmion lattice whose orientation is predominantly determined by the magnetic field direction and magnetocrystalline anisotropy [24,33–35]. As the crystalline axes of each grain are randomly oriented, the SANS pattern in the skyrmion phase becomes a generic ring in the plane perpendicular to the applied magnetic field. In a map of integrated SANS scattering intensity in powdered Cu_2OSeO_3 at the magnetic $|q| \approx 0.01$ Å^{-1} peak in the plane perpendicular to applied magnetic field, Fig. 2(b), the skyrmion phase and the multi-q helical phase both show azimuthally symmetric scattering intensity consistent with magnetization and published results [5,7,27] (within the SANS magnet calibration accuracy [36]), and are therefore not distinguishable in powders through their base SANS pattern alone [see Appendix B for details of magnetic peak fitting, and Appendix C for similar plot for $(Cu_{0.90}Zn_{0.10})_2OSeO_3$]. However, it has been shown that it is possible to collectively orient the skyrmion lattices and use SANS to distinguish a hexagonal skyrmion lattice phase from other helical phases oriented orthogonal to magnetic field [24]. In this procedure, a polycrystalline sample is prepared in a temperature/magnetic field environment which facilitates skyrmion formation, then the sample is rotated about the vertical axis (perpendicular to the magnetic field). After the rotation, the ring feature located at $|q| \approx 0.01$ Å^{-1} develops sixfold azimuthal symmetry, indicating long-range orientation of the skyrmion lattice. This can be seen in Fig. 3, where sixfold azimuthal symmetry is resolved in polycrystalline Cu_2OSeO_3 only after rotation in field. This same work also showed that rotating the sample outside of the skyrmion window resulted in a two-peak or uniform pattern. Note, however, that if no sixfold symmetry is observed after rotation, it is still possible that a skyrmion lattice phase is still present, but is pinned within each grain by magnetocrystalline anisotropy, surface anisotropy, or disorder.

TABLE I. Parameters used to fit $(Cu_{1-x}Zn_x)_2OSeO_3$ magnetization data to model Cu_2OSeO_3 magnetization data as per Eq. (E1). Uncertainties here represent a 95% confidence interval. Results of fit for each value of x_{Zn} shown in Fig. 12. For detailed discussion of fitting method, see Appendix E.

x_{Zn}	c_1	T_1	c_2	T_2
0.05	0.48 ± 0.03	-1.9 ± 0.2	0.46 ± 0.04	-8.5 ± 0.4
0.10	0.37 ± 0.02	-3.1 ± 0.2	0.52 ± 0.03	-12.2 ± 0.5

To quantify the skyrmion lattice alignment after rotation and highlight the hexagonal symmetry, the data are fit [black line in Figs. 3(c) and 3(d)] with six coupled Gaussian peaks:

$$I(\phi) = B + \sum_{n=1}^{3} A_n \left[e^{-\frac{\left[(\phi-\phi_0)-\frac{n\pi}{3}\right]^2}{2w_\phi}} + e^{-\frac{\left[(\phi-\phi_0)-\frac{n\pi}{3}-\pi\right]^2}{2w_\phi}} \right], \quad (1)$$

where B is a constant background, ϕ is the azimuthal coordinate, ϕ_0 is an azimuthal offset, w_ϕ is the width of the peak, and the three A_n are the height of each pair of opposing Gaussians. Reduced χ^2 for all fits to Eq. (1) are provided in Table II, along with the reduced χ^2 fit to an azimuthally uniform scattering profile.

Time-dependent relaxation of the sixfold symmetry back to azimuthal symmetry after rotation was observed in the substituted samples. The relaxation was observable on the timescale of minutes, consistent with previous observations of similar time-dependent lattice relaxations [14,20,21,34]. In the rotation measurements of substituted samples, scattering intensity was collected in bins of ≈ 30 s, and integrated for the time indicated in the caption, starting ≈ 10 s after rotation. The number of bins to integrate over was chosen to maximize the clarity of the sixfold symmetry, as longer counting improves statistics, although the peak intensity decreases with time.

The magnetization and SANS intensity maps of Fig. 2 allows direct confirmation of $|q| \approx 0.01$ Å^{-1} magnetic order perpendicular to magnetic field, while the rotation technique of Fig. 3 allows confirmation of sixfold symmetry due to a skyrmion lattice phase. Through a combination of these techniques, the magnetic phase diagram can be effectively mapped in polycrystalline samples. In what follows, these techniques are used together to characterize the magnetic structure of various chemical substitutions of Cu_2OSeO_3.

B. Silver and sulfur substitutions

Silver is substituted into the parent compound by substituting AgO for CuO in the initial composition, forming $(Cu_{1-x}Ag_x)_2OSeO_3$ with $x = 0.05$ and $x = 0.10$. The magnetic phase diagrams as determined by magnetometry (dM/dH) are shown in Figs. 4(a) and 4(b), while SANS data taken after the sample is rotated are shown in Figs. 4(c) and 4(d) for $x = 0.05$ and $x = 0.10$, respectively. Both substitutions show qualitatively similar results to the parent compound. The onset of magnetic order remains at ≈ 58 K. Additionally, both samples show enhancement of the low-field, multi-q helical phase stability with respect to magnetic field and a decrease in the saturation field. Sulfur is then substituted into the parent compound by replacing CuO with CuS to create $Cu_2(O_{1-x}S_x)_2SeO_2$ with $x = 0.05$ and $x = 0.10$. The magnetic phase diagrams are again shown in Figs. 4(e) and 4(f), while SANS data taken after the sample is rotated are shown in Figs. 4(g) and 4(h) for $x = 0.05$ and $x = 0.10$, respectively. The onset of magnetic order again remains within approximately 1 K of the original 58 K transition temperature. This behavior in $(Cu_{1-x}Ag_x)_2OSeO_3$ and $Cu_2(O_{1-x}S_x)_2SeO_2$ is in contrast to substitution studies in $Mn_{1-X}Fe_XSi$, $Mn_{1-X}Co_XSi$, and $Fe_{1-X}Co_XSi$ [37–41], where the transition temperature can be significantly suppressed by a comparable substitution level. As in the silver substitutions, the sulfur substitutions show similar enhancement of the low-field, multi-q helical phase, and suppression of the saturation field. Again, however, this saturation magnetization suppression is much weaker than is observed in other nonstoichiometric skyrmion compounds [37,38,40]. $M(T)$ at 100 mT is shown in Appendix A. In effect, chemical substitution of Ag or S appears to shrink the single-q helical phase region.

Remarkably, the dM/dH dip associated with skyrmion order becomes extended in temperature as both the Ag and the S substitution level is increased. The high temperature boundary of the skyrmion stability envelope remains relatively

TABLE II. Reduced χ^2 for fit of rotated SANS data to Eq. (1) versus fit to constant.

Compound	Figure (note)	χ^2/ν six peaks	χ^2/ν flat
Cu_2OSeO_3	Fig. 3(c) (before rotation)	0.84544	0.96155
Cu_2OSeO_3	Fig. 3(d) (after rotation)	0.91968	1.7138
$(Cu_{0.95}Ag_{0.05})_2OSeO_3$	Fig. 4(c)	0.95939	1.358
$(Cu_{0.9}Ag_{0.1})_2OSeO_3$	Fig. 4(d)	1.4856	1.6057
$Cu_2(O_{0.95}S_{0.05})_2SeO_2$	Fig. 4(g)	1.0094	1.3165
$Cu_2(O_{0.9}S_{0.1})_2SeO_2$	Fig. 4(h)	1.007	1.1116
$(Cu_{0.95}Zn_{0.05})_2OSeO_3$	Fig. 5(b)	0.97169	1.4223
$(Cu_{0.9}Zn_{0.1})_2OSeO_3$	Fig. 6(b) (high T)	0.92061	1.0003
$(Cu_{0.9}Zn_{0.1})_2OSeO_3$	Fig. 6(c) (low T)	1.7577	2.6191

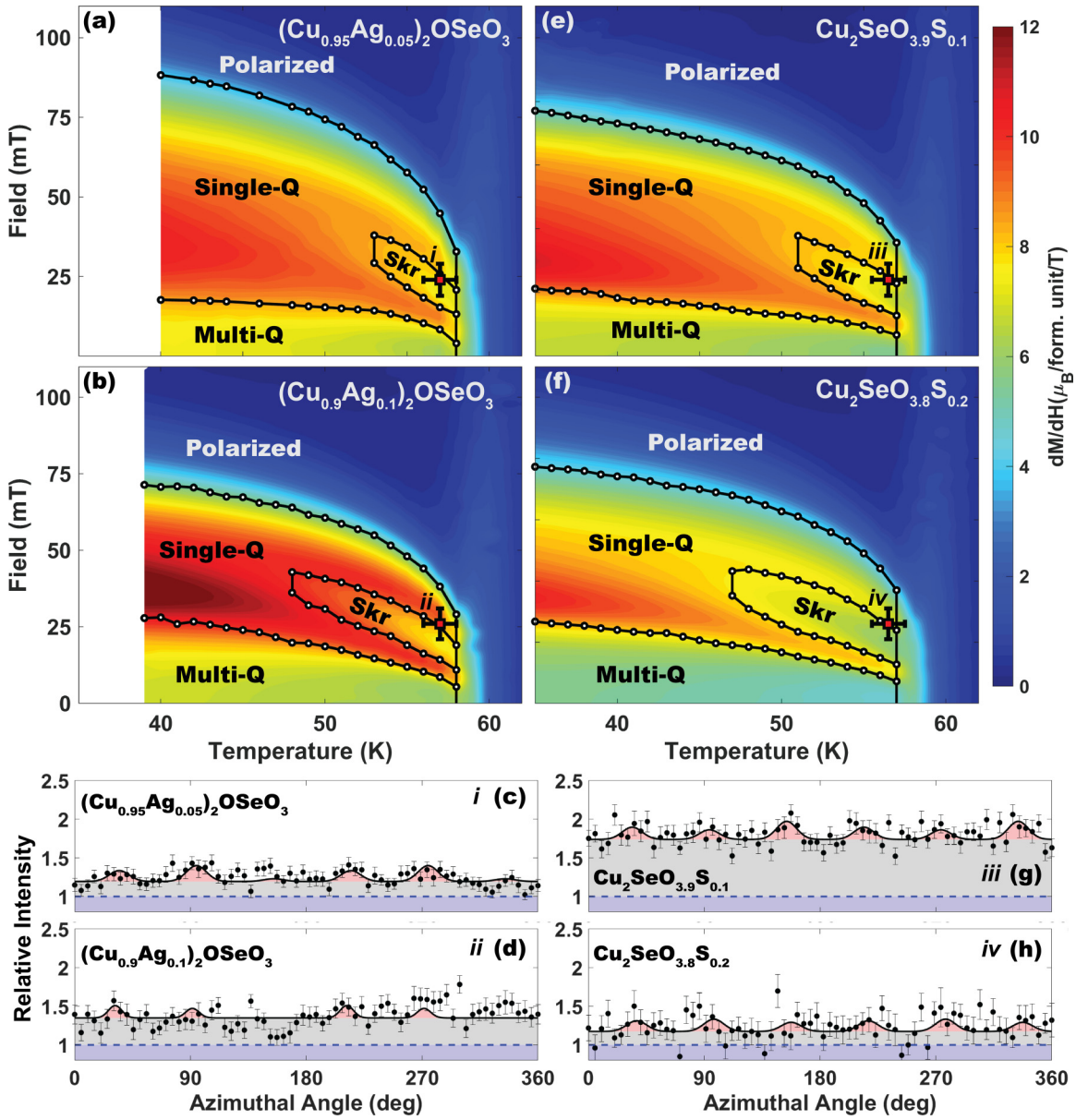

FIG. 4. dM/dH contour maps and SANS rotation measurements of polycrystalline $(Cu_{1-x}Ag_x)_2OSeO_3$ and $Cu_2(O_{1-x}S_x)_2SeO_2$. (a)–(d) $(Cu_{1-x}Ag_x)_2OSeO_3$ is shown on the left while (e)–(h) $Cu_2(O_{1-x}S_x)_2SeO_2$ is shown on the right. $x = 0.05$ is shown on top while $x = 0.10$ is shown on the bottom. The skyrmion region is broadened by increased substitution in both the Ag and S cases. Each SANS rotation plot represents the highest symmetry rotation pattern achieved after rotation around the vertical axis across a span of 180 deg approximately five times. (c), (d), (g), and (h) are integrated for 300, 220, 330, and 140 s, respectively. Temperature and field location of each rotation is indicated by a red square labeled with roman numerals i–iv corresponding to (c), (d), (g), and (h), respectively. Bars on the mark represent range of possible measurement conditions. In all cases, sixfold symmetry is observed, though increased substitution decreases the sixfold intensity. Phase boundaries were determined as they were for Cu_2OSeO_3 in Fig. 2.

unchanged with doping, but the skyrmion region extends to larger fields and lower temperatures with substitution. In both the Ag and S substitutions, the temperature range spans 10 K at $x = 0.10$. SANS measurements are consistent with the magnetometry results, showing sixfold symmetry after rotation in the skyrmion window [Figs. 4(c) and 4(d) and Figs. 4(g) and 4(h) for the Ag and S substitutions, respectively, see Table II for reduced χ^2]. SANS sixfold symmetry is plotted relative to the nuclear scattering contribution (see Appendix B). We do not observe a significant shift in helical pitch as measured by SANS, in contrast to substitution studies in $Mn_{1-X}Fe_XSi$ and $Fe_{1-X}Co_XSi$ [38,39,41]. Note that the ratio of magnetic scattering (gray) to nuclear scattering (blue) in the $x = 0.05$ sulfur substitution [Fig. 4(g)] is much larger than other substitutions, and is similar to the ratio of magnetic scattering to nuclear scattering seen in the parent [see Fig. 3(d)]. This suggests that the sulfur has a weaker effect on the magnetic order compared to other substitutions. Additionally, the skyrmion SANS signature is strongest towards the high temperature boundary of the skyrmion stability envelope, consistent with previous reports [26,27]. However, as evidenced in Fig. 4, increased substitution decreases the skyrmion

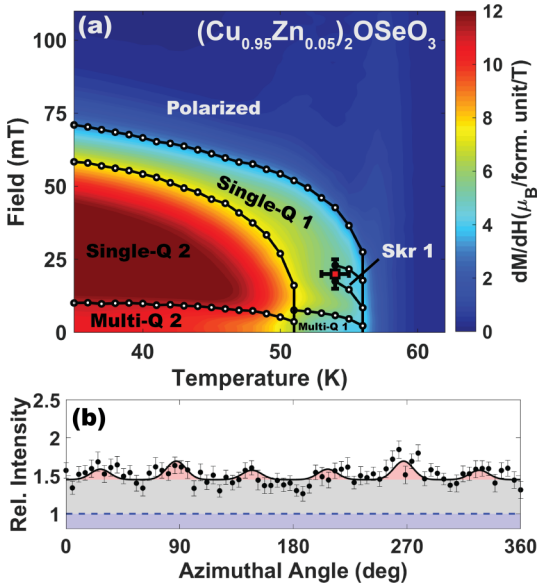

FIG. 5. Skyrmion phase in $(Cu_{0.95}Zn_{0.05})_2OSeO_3$. (a) The dM/dH magnetization contour plot for $(Cu_{0.95}Zn_{0.05})_2OSeO_3$. The phase boundaries, determined from the magnetization in the same way as the previous samples, are indicated with black lines. (b) An annular cut of a SANS measurement of the sample at the point indicated with a red square in (a) (bars on the mark represent range of possible measurement conditions). (b) Performed at 54 K and 20 mT for 240 s immediately after rotation, and shows weakened sixfold symmetry compared to the parent compound (see Fig. 3).

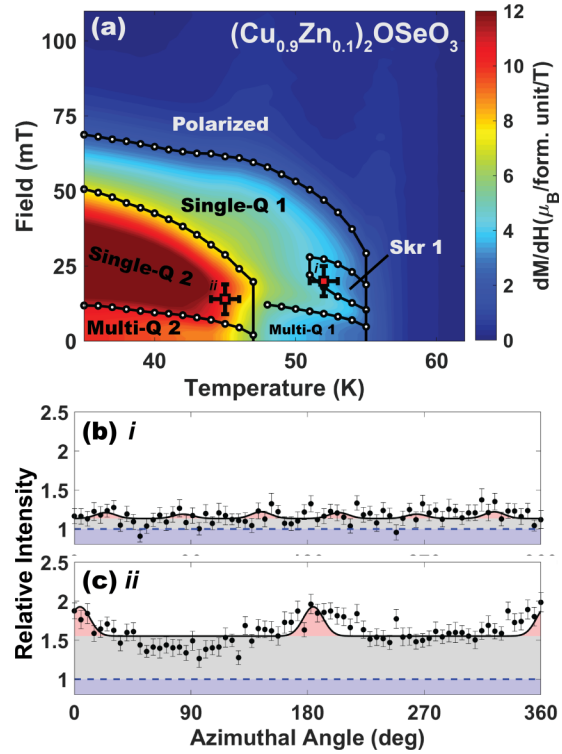

FIG. 6. Skyrmion phase in $(Cu_{0.90}Zn_{0.10})_2OSeO_3$. (a) The dM/dH magnetization contour plot for $(Cu_{0.90}Zn_{0.10})_2OSeO_3$. The phase boundaries, determined from the magnetization in the same way as the previous samples, are indicated with black lines. (b) and (c) Annular cuts of SANS measurements of the sample at the conditions—labeled i and ii, respectively—indicated with red squares in (a) (bars on the mark represent range of possible measurement conditions). (b) Performed at 52 K and 20 mT for 300 s after rotation while (c) is performed at 45 K and 14 mT for 420 s after rotation. (b) Shows weakened sixfold symmetry compared to the parent compound or $(Cu_{0.95}Zn_{0.05})_2OSeO_3$ (see Figs. 3 and 5). (c) No apparent ordered skyrmion lattice, instead favoring helical, twofold order.

lattice signature compared to the parent (as confirmed later in Fig. 7). Decreased scattering intensity can be the result of a reduced magnetic moment, or a change in the scattering form or structure factors. We expect here the decreased intensity to be the result of a reduced moment and structure factor. The reduced structure factor indicates increased disorder within the hexagonal skyrmion lattice, potentially due to local variations in the skyrmion pitch, pinning of the skyrmions during the lattice formation, or a coexistence of nonlattice skyrmions and helices.

These results show that both Ag and S substitution cause similar changes in the skyrmion phase diagram. We suggest that the underlying mechanism for this broadening is chemical disorder. In the case of the Ag substitution, the behavior could also be caused by change of valence or weakening of magnetic interaction strength as the magnetically active copper site is replaced. However, if the broadening were due to magnetic interactions, the sulfur substitution should not show the same behavior. Another alternative is that the substituted sample could possess some chemical phase splitting as is observed in Zn substituted samples [19]. However, we see no evidence of multiple magnetic transition temperatures in field polarized magnetization measurements in the Ag or S samples as we do in the Zn samples (Fig. 8). The broadening could also be due to chemical expansion as the substitutions expand the lattice. However, previous work has shown that positive applied pressure expands the skyrmion stability envelope while negative chemical pressure contracts it [16] in contradiction to the behavior seen here. Therefore, chemical disorder is the most likely cause.

C. Zinc substitution

Polycrystalline $(Cu_{1-x}Zn_x)_2OSeO_3$, as previously reported [18,19], shows strikingly different behavior from $(Cu_{1-x}Ag_x)_2OSeO_3$ or $Cu_2(O_{1-x}S_x)_2SeO_2$. Zn substitution creates a coexistence of two distinct stoichiometries within these powdered samples (as supported by previous reports of the different stoichiometries producing multiple nearby peaks in high-resolution x-ray powder diffraction [19]). Both stoichiometries demonstrate similar helimagnetic phase diagrams, but the nominally higher Zn concentration phase has a significantly lower transition temperature than the lower Zn concentration phase. The dM/dH phase diagram of $x = 0.05$ is shown in Fig. 5(a), and of $x = 0.10$ is shown in Fig. 6(a). Note that the $x = 0.05$ sample shows transitions at approximately 51 and 56 K while the $x = 0.10$ sample shows transitions at approximately 47 and 55 K. Thus, increasing Zn concentration lowers the transition temperature in both stoichiometries. The coexistence of these two magnetic transitions is clearly manifested as a kink in the magnetization as a function of temperature [Figs. 12(c) and 12(d) and Fig. 8(b)].

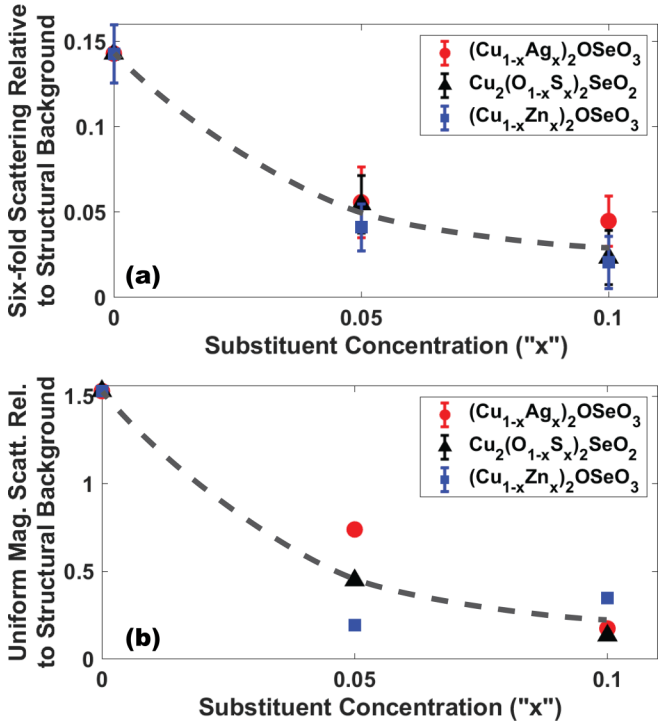

FIG. 7. Scaled magnetic SANS scattering intensity. (a) The ratio between the sixfold symmetric scattering intensity and the structural scattering intensity plotted as a function of concentration for $(Cu_{1-x}Zn_x)_2OSeO_3$, $(Cu_{1-x}Ag_x)_2OSeO_3$, and $Cu_2(O_{1-x}S_x)_2SeO_2$. The sixfold symmetric scattering can be attributed to the skyrmion phase. (b) The ratio between uniform magnetic scattering intensity and structural scattering intensity. The dashed lines are a guide to the eye. There is a general, monotonic decrease in skyrmion scattering intensity as substituent concentration is increased. Details of the calculation are given in Appendix B.

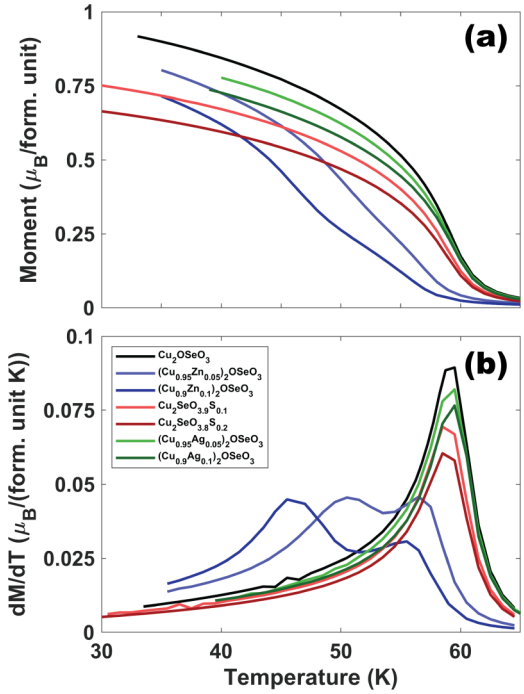

FIG. 8. Temperature T, dependence of magnetization M in the field-polarized state. (a) M of each substitution as a function of T at a constant field of 100 mT. (b) The derivative of (a) with respect to temperature, dM/dT.

The shift in temperature of T_C for each phase and approximate relative contribution of each stoichiometric phase is captured in Table I (see Appendix E for details of the magnetization analysis).

The rotation method (see Fig. 3 and associated discussion) allows further characterization of these skyrmion phases. Figure 5(b) and Figs. 6(b) and 6(c) show annular cuts of SANS data after rotation in the higher temperature candidate skyrmion phase in $(Cu_{0.95}Zn_{0.05})_2OSeO_3$ and the high and low temperature candidate skyrmion phases in $(Cu_{0.90}Zn_{0.10})_2OSeO_3$, respectively. Hexagonal symmetry is observed in both higher temperature skyrmion phases (refer to Table II for comparison of reduced χ^2), but weakens significantly as Zn concentration is increased. This can be associated with the increased substitution, as noted in Ag and S, and also with the volume fraction of the sample that contributes to the phase, which decreases significantly from Fig. 5(b) to 6(b) (see Table I). Indeed, plotting the integrated intensity of hexagonal scattering relative to the nuclear scattering as a function of substitution shows an overall decrease in the relative magnetic scattering intensity (Fig. 7). In contrast, rotating the $(Cu_{0.90}Zn_{0.10})_2OSeO_3$ sample in the lower temperature candidate skyrmion phase reveals a completely different behavior. After the rotation there is no apparent sixfold symmetry, but rather twofold symmetry across the rotation axis indicating helical order perpendicular to the rotation axis. This suggests that rotation in the proposed lower temperature skyrmion region promotes a helical state. Note however that it is possible that there is still a coexistence of nonlattice skyrmions or a dominance of the magnetocrystalline anisotropy or disorder pinning in determining the skyrmion lattice orientation even after rotation.

The fact that SANS shows helical order perpendicular to the magnetic field upon rotation in the lower temperature candidate skyrmion region also suggests that the helices are generally not as strongly aligned with the field direction as the helices in the parent Cu_2OSeO_3, where rotation aligns all helices with the field.

IV. CONCLUSION

Here we present results using magnetometry and SANS to study the effects of substitution at $x = \{0.05, 0.10\}$ in powdered $(Cu_{1-x}Zn_x)_2OSeO_3$, $(Cu_{1-x}Ag_x)_2OSeO_3$, and $Cu_2(O_{1-x}S_x)_2SeO_2$. We demonstrate the use of SANS to resolve skyrmion order in polycrystalline samples. While magnetization measurements indicate that Ag and S substitution enhances the temperature stability of the skyrmion phase, SANS measurements show reduced ordering of the skyrmion lattice with substitution. Additionally, while we show that the higher temperature stoichiometry in $(Cu_{0.90}Zn_{0.10})_2OSeO_3$ contains a skyrmion lattice phase, we do not see evidence of the second, lower temperature candidate skyrmion region. Chemical disorder induces disorder in the skyrmion lattices of Cu_2OSeO_3. This could manifest as a coexistence of skyrmion

and helical order as has been seen in thin films (Ref. [2], for example), or as a destruction of helical order entirely in parts of the system. Magnetic microscopy would prove enlightening to understanding the actual microstructure of these substitutions. Additionally, synthesis of single crystals or thin films with significant chemical substitution are still a worthy endeavor, and could improve sample homogeneity and reduce lattice disorder. Overall, these substitutions offer insight into the stability of skyrmion order in Cu_2OSeO_3, and may aid future developments in the technological applications of magnetic skyrmions.

ACKNOWLEDGMENTS

The authors would like to thank Paul Kienzle for support regarding SANS fitting; Jeffrey Krzywon, Tanya Dax, and Qiang (Alan) Ye for assistance with SANS instrumentation; Kefeng Wang and Halyna Hodovanets for help with growth procedures; Philip Piccoli for WDS measurements; and Juscelino Leão for useful discussion of data analysis. Support for Paul Neves was provided by the Center for High Resolution Neutron Scattering, a partnership between the National Institute of Standards and Technology and the National Science Foundation under Agreement No. DMR-1508249. Additionally, we acknowledge the support of the National Institute of Standards and Technology, U.S. Department of Commerce, in providing the neutron research facilities used in this work. Certain commercial materials are identified in this paper to foster understanding. Such identification does not imply recommendation or endorsement by the National Institute of Standards and Technology, nor does it imply that the materials or equipment identified are necessarily the best available for the purpose.

The authors report no conflicts of interest in this investigation.

APPENDIX A: SATURATION MAGNETIZATION

Magnetization M, as a function of temperature T, is shown for each substitution studied above in Fig. 8(a). All 100 mT magnetization values were extracted from field sweeps from -4 to 100 mT at constant temperature so as to be in the field-polarized state. The parent compound shows the highest saturation magnetization, while increasing substitution lowers the saturation magnetization. This lowering saturation magnetization is expected when substituting the magnetically active site with nominally nonmagnetic Ag and Zn. The derivative of M with respect to T, dM/dT, is given in Fig. 8(b). A peak in dM/dT corresponds to the magnetic transition temperature. The Ag and S substitutions show little change in the onset of magnetic order. However, the zinc substitutions show two peaks in dM/dT for the two stoichiometries as discussed above and in previous work [19].

APPENDIX B: SANS ANALYSIS

Here we outline the analysis that leads to our results on skyrmion SANS intensity as presented in Figs. 2(b), 7, 10, and the related discussion.

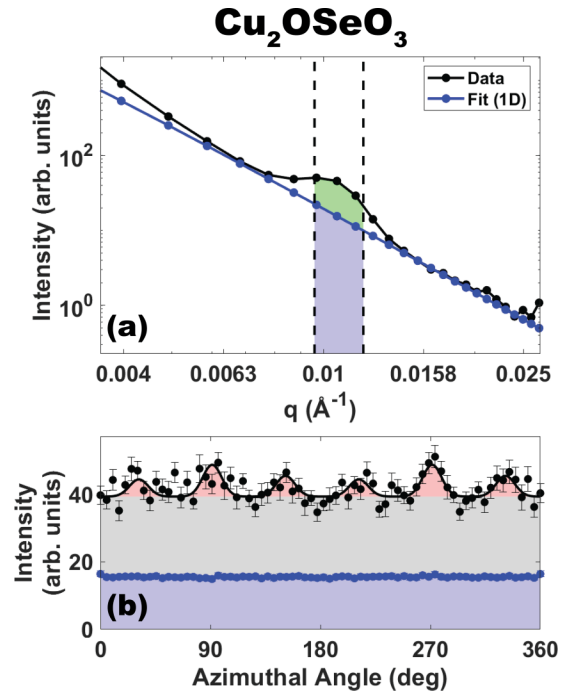

FIG. 9. Guide to SANS analysis. Data for polycrystalline parent Cu_2OSeO_3 in the skyrmion state at 57 K after rotation [as shown in Fig. 3(b)] used here for clarity. (a) Intensity of SANS as a function of q (black). A large structural background due to the powder granules is fit with a model function (blue). This allows isolation of the magnetic peak integrated intensity centered near $|q| \approx 0.01$ Å^{-1}. (b) SANS intensity as a function of azimuthal angle within the q range indicated by black dashed vertical lines in (a). Rotation of the sample in magnetic field precipitates sixfold symmetry in the data (black), while the model structural scattering leads to a uniform, lower intensity background (blue). The structural scattering intensity is shaded light blue, uniform magnetic scattering is shaded gray, and sixfold symmetric magnetic scattering is shaded red. The ratio of sixfold symmetric integrated intensity to structural background integrated intensity is a figure of merit for skyrmion lattice order.

To generate the field-perpendicular helimagnetic scattering intensity maps shown in Figs. 2(b) and 10, SANS measurements were performed at a variety of temperature and field conditions. The sample was saturated in a field of ≈ 0.3 T to the field polarized state after each temperature change. The black $I(q)$ plotted in Fig. 9(a) shows exemplary helimagnetic scattering observed in the parent skyrmion phase. Each SANS $I(q)$ data set is fit with a Markov chain Monte Carlo fitting algorithm using Bumps [42,43]. A Guinier-Porod function [44] is used to empirically model the powder grain nuclear scattering, and a Gaussian peak is added to empirically model the helimagnetic scattering centered at $|q| \approx 0.01$ Å^{-1}. Then, the integrated intensity of the Gaussian peak is plotted for each $I(q)$ as a function of temperature and field. This maps the field-perpendicular helimagnetic scattering as a function of temperature and field.

To generate Fig. 7 we performed a separate but related analysis of the SANS pattern after rotation. First, we modeled the nuclear scattering in $I(q)$ with a power-law function [blue in Fig. 9(a)]. (The Guinier-Porod nuclear scattering model

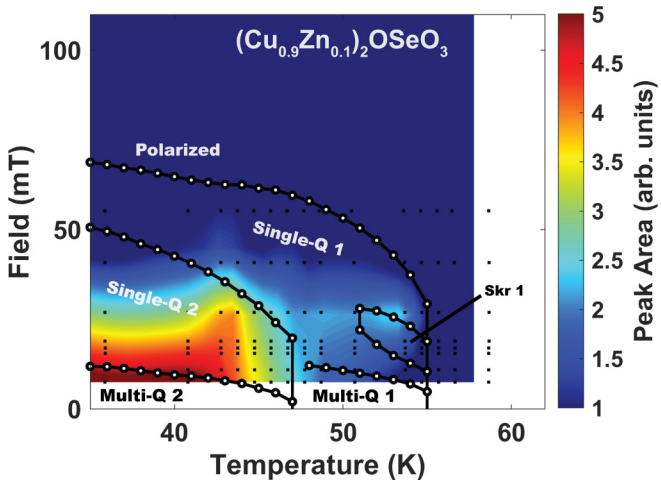

FIG. 10. $|q| \approx 0.01$ Å^{-1} magnetic peak SANS integrated intensity map of helical order perpendicular to applied magnetic field as a function of temperature and field strength in polycrystalline $(Cu_{0.90}Zn_{0.10})_2OSeO_3$ [analogous to Fig. 2(b)]. Field is applied parallel to the incident neutron beam. Measurements are taken at many temperatures and fields (shown with black points). Integrated scattering intensity due to the $|q| \approx 0.01$ Å^{-1} magnetic peak corresponding to out-of-plane helical order is determined from fitting the magnetic peak on top of a structural, power-law background. Phase boundaries determined from magnetization measurements [Fig. 6(a)] are shown. A maximum in intensity is seen corresponding to Skr 1 at 53 K and 27 mT. Large, field-perpendicular helical intensity is also visible at low temperature and field due to the helical phase. No peak in intensity can be resolved corresponding to the reported lower temperature skyrmion region.

is unnecessary here as the magnetic scattering at the center of the skyrmion phase after rotation is sufficiently strong to allow for a less sophisticated model). The data (black) and model (blue) integrated intensity within the selected skyrmion q range [indicated in Fig. 9(a) with vertical dashes] is plotted as a function of azimuthal angle in Fig. 9(b). These q bounds are chosen as they generate the clearest sixfold symmetry in the data. The power-law model in Fig. 9(a) is used to determine the azimuthally uniform, nuclear contribution (blue points) to the signal in Fig. 9(b), and allows calculation of the nuclear scattering integrated intensity within this q range. The data (black points) show sixfold symmetric scattering from skyrmion order precipitated by the rotation (red), and isotropic helimagnetic and nonlattice skyrmion scattering (gray) on top of the nuclear scattering (blue). The data are fit (reduced χ^2 provided in Table II, and compared to reduced χ^2 of an azimuthally uniform scattering profile) with Eq. (1) to obtain the integrated intensity of the sixfold symmetric scattering and the nonsixfold scattering. Then the ratio of the sixfold scattering intensity to the nuclear scattering intensity [red area to blue area in Fig. 9(b)] can be plotted as a function of substituent concentration [Fig. 7(a)]. This ratio offers a figure of merit for the amount of scattering due to ordered skyrmion lattices, normalized by the nuclear background. This normalizes intensity scaling due to varied sample mass in the neutron beam among samples. Similarly, the ratio of the uniform magnetic scattering intensity to the nuclear scattering intensity [*gray* area to blue area in Fig. 9(b)] is plotted in the exact same way in Fig. 7(b).

It is also possible to isolate the magnetic scattering from the nuclear scattering by subtracting a high temperature or high field background measurement, then fitting the area of the peak centered at $|q| \approx 0.01$ Å^{-1}. Both directly fitting the nuclear scattering and subtracting a background measurement give qualitatively similar results. However, this background subtraction method does not isolate the helimagnetic scattering quite as well as the fitting method presented here. There is a field-dependent contribution to the background scattering, as spins in each granule paramagnetically align with the field, that follows the same q dependence as the nuclear powder scattering in directions perpendicular to the magnetic field. Simple background subtraction does not fully capture all the details of this magnetic field-dependent scattering.

APPENDIX C: Zn SUBSTITUTION SANS MAGNETIC SCATTERING

The magnetic phase diagram for polycrystalline $(Cu_{0.90}Zn_{0.10})_2OSeO_3$ in Fig. 6(a) is supported by a mapping (Fig. 10) of the SANS field-perpendicular helimagnetic scattering at $|q| \approx 0.01$ Å^{-1}, as was done for the parent Cu_2OSeO_3 in Fig. 2(b). Figure 10 shows a peak in field-perpendicular helimagnetic scattering at 53 K and 25 mT corresponding to Skr 1. This plot also shows strong field-perpendicular helical order in the low temperature single-q helical phase in comparison to the parent single-q helical phase. This is consistent with the behavior of $(Cu_{0.90}Zn_{0.10})_2OSeO_3$ SANS under field rotations in this region [Fig. 6(c)]. This suggests that disorder causes the

TABLE III. Quantitative analysis of x-ray powder diffraction measurements presented in Fig. 11. Asterisked phase fractions indicate the presence of unidentified peaks and/or unavailable RIR values for some identified impurity phases. The impurity peaks in $Cu_2(O_{0.9}S_{0.1})_2SeO_2$ precluded any meaningful phase fraction quantization.

Compound	Phase fraction	Lattice constant (Å)
Cu_2OSeO_3	0.99	8.926(1)
$(Cu_{0.95}Ag_{0.05})_2OSeO_3$	0.96	8.926(6)
$(Cu_{0.9}Ag_{0.1})_2OSeO_3$	0.86	8.934(4)
$Cu_2(O_{0.95}S_{0.05})_2SeO_2$	0.85*	8.923(3)
$Cu_2(O_{0.9}S_{0.1})_2SeO_2$	–*	8.926(8)
$(Cu_{0.95}Zn_{0.05})_2OSeO_3$	0.97	8.928(2)
$(Cu_{0.9}Zn_{0.1})_2OSeO_3$	0.97	8.934(3)

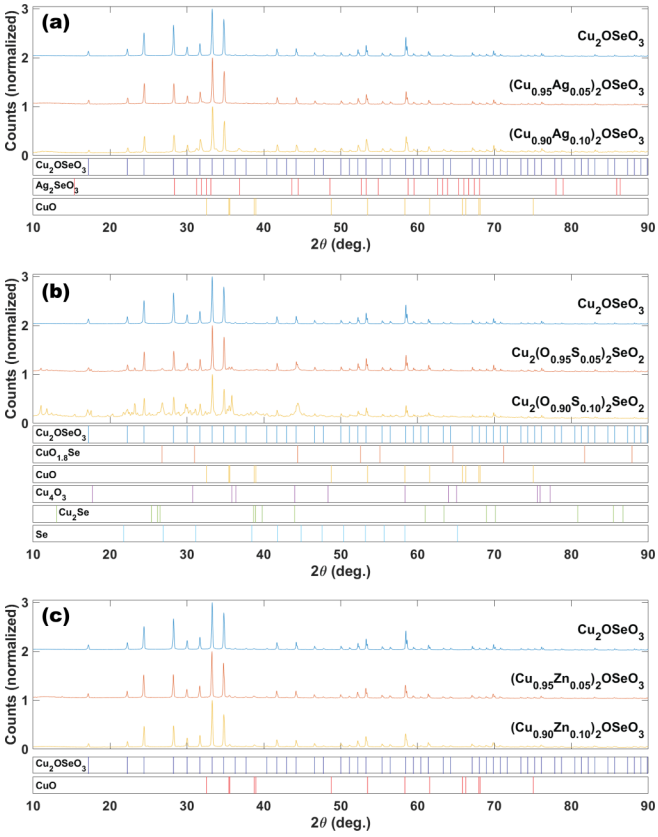

FIG. 11. X-ray powder diffraction patterns of (a) silver substituted samples, (b) sulfur substituted samples, and (c) zinc substituted samples. Reference reflections are provided below each plot for identified phases present. Quantitative results of measurement are listed in Table III.

helices in the second, lower temperature helical phase to be less polarized along the field direction, leading to greater field-perpendicular helimagnetic ordering. It is possible that the increased intensity at lower temperatures could be due partially to a second skyrmion stability window as has been recently reported [10,11,13], though no hexagonal pattern was observed in the SANS data before or after rotation in this region. Additionally, the field-perpendicular helical order below the second transition is much stronger than that in the Skr 1 region because Skr 1 is only present in approximately one half of the sample (see Table I), while the helical order is nominally full volume fraction below the second transition. The SANS intensity due to the skyrmions is thus about half as intense as the full-volume helical intensity, as expected.

APPENDIX D: SAMPLE CHARACTERIZATION

X-ray powder diffraction was measured on all samples in order to determine phase purity. Diffraction patterns are shown in Fig. 11, and quantitative analysis is shown in Table III. All measurements were obtained on a Rigaku Miniflex benchtop powder x-ray diffractometer. Displayed reference reflections in Fig. 11 correspond to the following International Centre for Diffraction Data reference codes: 00-046-0793 for Cu_2OSeO_3, 04-013-3985 for Ag_2SeO_3, 04-007-1375 for CuO, 04-004-7717 for $Cu_{1.8}Se$, 04-008-4362 for Cu_4O_3, 00-037-1187 for Cu_2Se, and 00-032-0992 for Se. The phase fraction of the target phase was determined through a standard semi-quantitative analysis procedure performed by the HighScore Plus crystallography software package. This analysis identifies the relative mass fractions of each identified phase by comparing to calibrated reference intensity ratios (RIR) diffraction patterns. Notably, when unidentified peaks or reference patterns with no RIR score are present in a sample, this analysis method will overestimate all phase fraction estimates. This is relevant in the sulfur substitutions.

Increased substitution appears to slightly increase observed lattice constants, and decrease the fraction of target phase. Notably, increasing sulfur substitution promotes the formation of several impurity phases which limit the accurate quantification of phase fraction in Table III. We do not see evidence of any known magnetic transitions due to any known [45–47] impurity phases in the magnetization (Fig. 8) of the 10% S substituted samples, suggesting that the dominant magnetic order is due to the target phase.

Finally, we also include wavelength-dispersive x-ray spectroscopy (WDS) measurements on a number of grains of the $(Cu_{0.9}Zn_{0.1})_2OSeO_3$ sample in Table IV. We see some evidence of zinc concentration inhomogeneity, which is consistent with our magnetization data and previous work [19]. The zinc substitution fraction X_{Zn} (defined as the stoichiometric ratio of zinc to zinc plus copper), has a range of 0.067, a mean value of 0.081, and a standard deviation of 0.022.

TABLE IV. Wavelength-dispersive x-ray spectroscopy (WDS) measurements of (nominally) $(Cu_{0.9}Zn_{0.1})_2OSeO_3$ for multiple powder grains. Relative chemical concentrations are normalized to the oxygen concentration in the sample. The zinc substitution fraction X_{Zn} given as the stoichiometric ratio of zinc to zinc plus copper, is also given.

No.	Cu	Zn	Se	O	X_{Zn}
1	2.169	0.167	0.833	4	0.071
2	1.934	0.144	0.961	4	0.069
3	1.976	0.200	0.912	4	0.092
4	1.865	0.211	0.962	4	0.102
5	1.975	0.129	0.948	4	0.061
6	1.832	0.165	1.002	4	0.083
7	1.807	0.203	0.995	4	0.101
8	2.141	0.094	0.883	4	0.042
9	1.893	0.231	0.938	4	0.109

APPENDIX E: Zn MAGNETIZATION ANALYSIS

To further establish that the magnetization of the Zn substituted samples is well explained by the coexistence of two stoichiometries, we use the magnetization data of Cu_2OSeO_3, $M_{\text{parent}}(T, H)$, which exhibits the largest saturation magnetization [see black curve in Appendix A, Fig. 8(a)], as a functional form to qualitatively model the Zn substituted magnetization data, $M_{\text{Zn}}(T, H)$ [also shown in Fig. 8(a)]. The shifting transition temperatures and the volume fraction of each stoichiometry within a sample are accommodated in the model as

$$M_{\text{Zn}}(T, H) \approx c_1 M_{\text{parent}}(T - T_1, H) + c_2 M_{\text{parent}}(T - T_2, H). \tag{E1}$$

T_i is the transition temperature shift and c_i is the fractional contribution, relative to the parent saturation magnetization, of each stoichiometry within the sample. $M_{\text{parent}}(T, H)$ is used as a model to emphasize the distinct phases, not to capture all details of the phase diagram perfectly. The model is fit to the data along $M_{Zn}(T, H = 100\ \text{mT})$ [shown in Fig. 8(a)] so as to consider only the transition from the paramagnetic to the field-polarized state in each of the two distinct stoichiometries within the sample and not the more nuanced helimagnetic phases. These fits of $M_{\text{Zn}}(T, H = 100\ \text{mT})$, shown in Figs. 12(c) and 12(d), obtain reduced χ^2 of 0.22 and 0.45 for $x_{\text{Zn}} = 0.05$ and $x_{\text{Zn}} = 0.10$, respectively. The fit parameters are given in Table I. These parameters characterize the volume fraction and temperature shifts of two distinct phases within $(Cu_{1-x}Zn_x)_2OSeO_3$.

The magnetic phase diagrams in dM/dH generated from this model of $M(T, H = 100\ \text{mT})$ are shown in Figs. 12(a) and 12(b). The agreement between these phase diagram models and the data in Figs. 5(a) and 6(a) is excellent, with the exception of the low temperature skyrmion region as discussed later. Thus these polycrystalline, Zn-substituted samples can be treated as containing two distinct stoichiometries with different Zn concentrations, leading to a superposition of two helimagnetic phase diagrams with separate transition temperatures dictated by the Zn concentration (with the lower temperature phase likely containing more Zn). These two stoichiometries must have the same crystal structure but with different Zn substitution levels, as x-ray powder diffraction does not reveal a second crystal structure within the sample. It is possible that the segregation of regions with different Zn substitution levels is as small as submicron, however spatially resolved compositional analysis would be required to determine the real-space distribution of these domains. Admittedly, this model does not fully capture all details of the magnetic phase diagram below the field polarized state—particularly the lower saturation field of the substituted samples. However, using $Cu_2(O_{0.95}S_{0.05})_2SeO_2$ as a model in the same way as above (not shown) results in even better modeling of the magnetic phase diagram, suggesting there are similar chemical disorder-induced effects in the Zn phase diagram, as was noted for the Ag and S substitutions.

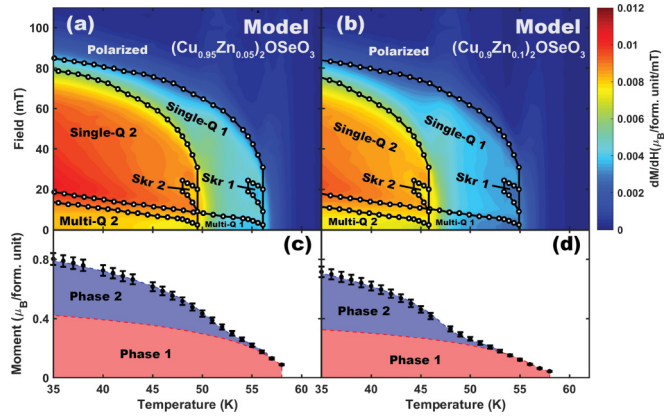

FIG. 12. Modeling the magnetization of $(Cu_{1-x}Zn_x)_2OSeO_3$. (a) and (b) Attempt to replicate the actual magnetization of $(Cu_{1-x}Zn_x)_2OSeO_3$ with the superposition of two identical, weighted, temperature-shifted, magnetization measurements for Cu_2OSeO_3 as described in Eq. (E1) with parameters given in Table I. Phase boundaries for each data set are indicated with black boundaries. This modeling of the Zn magnetization replicates many of the important features found in Figs. 5(a) and 6(a), and suggests that the Zn substitutions are well described by two partial volume fractions of different stoichiometries, creating two different superimposed magnetic phase diagrams. (c) and (d) The real magnetization of each Zn sample (black) as a function of temperature at a constant field of 100 mT. There are two magnetic transition temperatures as the sample transitions from paramagnetic to field polarized. The contribution to M from the first model phase is shown in red, while the contribution from the second model phase is shown in blue. The sum of the two model phases (red and blue) closely resembles the actual magnetization (black).

[1] S. Mühlbauer, B. Binz, F. Jonietz, C. Pfleiderer, A. Rosch, A. Neubauer, R. Georgii, and P. Böni, Science **323**, 915 (2009).

[2] X. Yu, Y. Onose, N. Kanazawa, J. Park, J. Han, Y. Matsui, N. Nagaosa, and Y. Tokura, Nature (London) **465**, 901 (2010).

[3] U. Rößler, A. Bogdanov, and C. Pfleiderer, Nature (London) **442**, 797 (2006).

[4] A. Fert, V. Cros, and J. Sampaio, Nat. Nanotechnol. **8**, 152 (2013).

[5] S. Seki, X. Yu, S. Ishiwata, and Y. Tokura, Science **336**, 198 (2012).

[6] T. Adams, A. Chacon, M. Wagner, A. Bauer, G. Brandl, B. Pedersen, H. Berger, P. Lemmens, and C. Pfleiderer, Phys. Rev. Lett. **108**, 237204 (2012).

[7] Y. Onose, Y. Okamura, S. Seki, S. Ishiwata, and Y. Tokura, Phys. Rev. Lett. **109**, 037603 (2012).

[8] J. S. White, I. Levatić, A. Omrani, N. Egetenmeyer, K. Prša, I. Živković, J. L. Gavilano, J. Kohlbrecher, M. Bartkowiak, H. Berger *et al.*, J. Phys.: Condens. Matter **24**, 432201 (2012).

[9] W. Jiang, P. Upadhyaya, W. Zhang, G. Yu, M. B. Jungfleisch, F. Y. Fradin, J. E. Pearson, Y. Tserkovnyak, K. L. Wang, O. Heinonen *et al.*, Science **349**, 283 (2015).

[10] A. Chacon, L. Heinen, M. Halder, A. Bauer, W. Simeth, S. Mühlbauer, H. Berger, M. Garst, A. Rosch, and C. Pfleiderer, Nat. Phys. **14**, 936 (2018).

[11] F. Qian, L. J. Bannenberg, H. Wilhelm, G. Chaboussant, L. M. Debeer-Schmitt, M. P. Schmidt, A. Aqeel, T. T. Palstra, E. Brück, A. J. Lefering *et al.*, Sci. Adv. **4**, eaat7323 (2018).

[12] M. Halder, A. Chacon, A. Bauer, W. Simeth, S. Mühlbauer, H. Berger, L. Heinen, M. Garst, A. Rosch, and C. Pfleiderer, Phys. Rev. B **98**, 144429 (2018).

[13] L. J. Bannenberg, H. Wilhelm, R. Cubitt, A. Labh, M. P. Schmidt, E. Lelièvre-Berna, C. Pappas, M. Mostovoy, and A. O. Leonov, npj Quantum Mater. **4**, 1 (2019).

[14] A. Bauer, A. Chacon, M. Wagner, M. Halder, R. Georgii, A. Rosch, C. Pfleiderer, and M. Garst, Phys. Rev. B **95**, 024429 (2017).

[15] K. D. Chandrasekhar, H. Wu, C. Huang, and H. Yang, J. Mater. Chem. C **4**, 5270 (2016).

[16] H. Wu, K. Chandrasekhar, T. Wei, K. Hsieh, T. Chen, H. Berger, and H. Yang, J. Phys. D **48**, 475001 (2015).

[17] M.-G. Han, J. Garlow, Y. Kharkov, L. Camacho, R. Rov, J. Sauceda, G. Vats, K. Kisslinger, T. Kato, O. Sushkov *et al.*, Sci. Adv. **6**, eaax2138 (2020).

[18] H. Wu, T. Wei, K. Chandrasekhar, T. Chen, H. Berger, and H. Yang, Sci. Rep. **5**, 13579 (2015).

[19] A. Štefančič, S. H. Moody, T. J. Hicken, M. T. Birch, G. Balakrishnan, S. A. Barnett, M. Crisanti, J. S. O. Evans, S. J. R. Holt, K. J. A. Franke, P. D. Hatton, B. M. Huddart, M. R. Lees, F. L. Pratt, C. C. Tang, M. N. Wilson, F. Xiao, and T. Lancaster, Phys. Rev. Mater. **2**, 111402(R) (2018).

[20] M. N. Wilson, M. Crisanti, C. Barker, A. Štefančič, J. S. White, M. T. Birch, G. Balakrishnan, R. Cubitt, and P. D. Hatton, Phys. Rev. B **99**, 174421 (2019).

[21] M. T. Birch, R. Takagi, S. Seki, M. N. Wilson, F. Kagawa, A. Štefančič, G. Balakrishnan, R. Fan, P. Steadman, C. J. Ottley, M. Crisanti, R. Cubitt, T. Lancaster, Y. Tokura, and P. D. Hatton, Phys. Rev. B **100**, 014425 (2019).

[22] M. Birch, S. Moody, M. Wilson, M. Crisanti, O. Bewley, A. Štefančič, G. Balakrishnan, R. Fan, P. Steadman, D. A. Venero *et al.*, Phys. Rev. B **102**, 104424 (2020).

[23] A. S. Sukhanov, P. Vir, A. S. Cameron, H. C. Wu, N. Martin, S. Mühlbauer, A. Heinemann, H. D. Yang, C. Felser, and D. S. Inosov, Phys. Rev. B **100**, 184408 (2019).

[24] D. A. Gilbert, A. J. Grutter, P. M. Neves, G.-J. Shu, G. Zimanyi, B. B. Maranville, F.-C. Chou, K. Krycka, N. P. Butch, S. Huang *et al.*, Phys. Rev. Mater. **3**, 014408 (2019).

[25] J.-W. G. Bos, C. V. Colin, and T. T. M. Palstra, Phys. Rev. B **78**, 094416 (2008).

[26] K. Makino, J. D. Reim, D. Higashi, D. Okuyama, T. J. Sato, Y. Nambu, E. P. Gilbert, N. Booth, S. Seki, and Y. Tokura, Phys. Rev. B **95**, 134412 (2017).

[27] S. Seki, J.-H. Kim, D. S. Inosov, R. Georgii, B. Keimer, S. Ishiwata, and Y. Tokura, Phys. Rev. B **85**, 220406(R) (2012).

[28] Y. Tokunaga, X. Yu, J. White, H. M. Rønnow, D. Morikawa, Y. Taguchi, and Y. Tokura, Nat. Commun. **6**, 7638 (2015).

[29] S. Woo, K. Litzius, B. Krüger, M.-Y. Im, L. Caretta, K. Richter, M. Mann, A. Krone, R. M. Reeve, M. Weigand *et al.*, Nat. Mater. **15**, 501 (2016).

[30] M. C. Langner, S. Roy, S. K. Mishra, J. C. T. Lee, X. W. Shi, M. A. Hossain, Y. D. Chuang, S. Seki, Y. Tokura, S. D. Kevan, and R. W. Schoenlein, Phys. Rev. Lett. **112**, 167202 (2014).

[31] Y. Yamasaki, D. Morikawa, T. Honda, H. Nakao, Y. Murakami, N. Kanazawa, M. Kawasaki, T. Arima, and Y. Tokura, Phys. Rev. B **92**, 220421(R) (2015).

[32] S. I. Zhang, A. Bauer, H. Berger, C. Pfleiderer, G. van der Laan, and T. Hesjedal, Phys. Rev. B **93**, 214420 (2016).

[33] T. Adams, M. Garst, A. Bauer, R. Georgii, and C. Pfleiderer, Phys. Rev. Lett. **121**, 187205 (2018).

[34] L. J. Bannenberg, F. Qian, R. M. Dalgliesh, N. Martin, G. Chaboussant, M. Schmidt, D. L. Schlagel, T. A. Lograsso, H. Wilhelm, and C. Pappas, Phys. Rev. B **96**, 184416 (2017).

[35] W. Münzer, A. Neubauer, T. Adams, S. Mühlbauer, C. Franz, F. Jonietz, R. Georgii, P. Böni, B. Pedersen, M. Schmidt *et al.*, Phys. Rev. B **81**, 041203(R) (2010).

[36] The resistive magnet calibration has several sources of uncertainty when determining the absolute field strength including deviation between where the magnet was calibrated and where the sample was located once installed, and hysteresis in the ferromagnetic yokes of the magnet. This could account for the slight discrepancy in field values between the magnetometer and the SANS magnet. We wish to point out that the center of mass of the SANS feature is displaced by only 3.75 mT, which is reasonable for our field uncertainty. The SANS feature is expected to be larger than the magnetometry defined window since the skyrmions do not spontaneously disappear across the sample at the field boundary. Variations in energies such as pinning defect sites, surface, magnetostatic and anisotropy energies broadens the annihilation field within the sample, and will be distributed especially in a powder. By comparison, the boundary is defined by the local extremal $d2M/dH2$, which is well defined.

[37] A. Bauer, A. Neubauer, C. Franz, W. Münzer, M. Garst, and C. Pfleiderer, Phys. Rev. B **82**, 064404 (2010).

[38] A. Bauer, M. Garst, and C. Pfleiderer, Phys. Rev. B **93**, 235144 (2016).

[39] L. J. Bannenberg, R. M. Dalgliesh, T. Wolf, F. Weber, and C. Pappas, Phys. Rev. B **98**, 184431 (2018).

[40] L. J. Bannenberg, F. Weber, A. J. E. Lefering, T. Wolf, and C. Pappas, Phys. Rev. B **98**, 184430 (2018).

[41] S. V. Grigoriev, V. A. Dyadkin, E. V. Moskvin, D. Lamago, T. Wolf, H. Eckerlebe, and S. V. Maleyev, Phys. Rev. B **79**, 144417 (2009).

[42] P. A. Kienzle, J. Krycka, N. Patel, and I. Sahin, Bumps (Version 0.7.11) [Computer Software]. College Park, MD: University of Maryland (2011), https://bumps.readthedocs.io/en/latest/getting_started/license.html#credits.

[43] J. A. Vrugt, J. M. Hyman, B. A. Robinson, D. Higdon, C. Ter Braak, J. F. Cajo, and C. G. H. Diks, Int. J. Nonlinear Sci. Numer. Simul. (2008), https://www.osti.gov/biblio/960766.

[44] B. Hammouda, J. Appl. Crystallogr. **43**, 716 (2010).

[45] O. Kondo, M. Ono, E. Sugiura, K. Sugiyama, and M. Date, J. Phys. Soc. Jpn. **57**, 3293 (1988).

[46] L. Pinsard-Gaudart, J. Rodriguez-Carvajal, A. Gukasov, and P. Monod, Phys. Rev. B **69**, 104408 (2004).

[47] A. Hamzić, Z. Ogorelec, K. Zadro, and M. Basletić, J. Magn. Magn. Mater. **233**, 181 (2001).